PCCP

Accepted Manuscript

ROYAL SOCIETY OF CHEMISTRY

www.rsc.org/pccp

PCCP

ARTICLE

Density functional study on the hole doped single-layer SnS_2 with metal element X- (Li, Mg, Al)

Received 00th January 20xx,
Accepted 00th January 20xx

DOI: 10.1039/x0xx00000x

www.rsc.org/

Dandan Yu, Yanyu Liu, Lili Sun, Ping Wu, Wei Zhou*

The effects of metal element X-doping on the electronic and optical properties of single-layer SnS_2 were investigated based on density functional theory. The results show that the doping is energetically favorable under S-rich conditions than under Sn-rich conditions. For Li and Mg doping, there is existence of ionic bonding between the dopants and adjacent S atoms, and the systems exhibit magnetic ground states. However, a covalent bonding character is observed in Al-doped single-layer SnS_2, and the system exhibits non-magnetic ground states. The results of optical properties show that the optical absorptions are anisotropic for all doping cases. The X doping not only results in the red shift of absorption edges, but also enhances the effective utilization in the near-infrared light region. Additionally, the Li-doped single-layer SnS_2 can be active for overall water splitting under visible light radiation whereas Mg and Al-doped SnS_2 are only suitable for oxygen evolution.

1. Introduction

In recent years, the graphene with two-dimensional (2D) honeycomb structure has received particular attention because of its outstanding thermal conductivity, high charge mobility, and excellent mechanical properties.[1-5] However, its intrinsic "zero band-gap" characteristic hinders its applications in the fields of semiconductor devices and integrated circuits.[3] Therefore, many researchers have focused on developing the novel materials that not only have analogous graphene layered organization, but also exhibit the excellent band structures, such as BN,[6,7] GaN,[8] GaS,[9] SnS_2,[10-12] and MoS_2.[13-15] Among them, being earth-abundant, nontoxic, and environment-friendly semiconductor, SnS_2 has been widely reported for applications in lithium battery, water splitting, and field effect transistor.[16-19] In particular, due to its band gap of 2.18-2.44 eV and good stability in acid and neutral aqueous solution,[17,18] SnS_2 is currently thought to be a fascinating candidate for visible light sensitive photocatalyst.

Experimentally, SnS_2 with 2D structure has been synthesized, such as nanoparticles, nanoplates and nanosheets.[20-23] Especially, the single-layer SnS_2 exhibits more preeminent photocatalytic properties in comparison with their three-dimensional (3D) counterparts. For instance, Sun *et al.*[22] synthesized SnS_2 single-layers with three atom thickness and observed that the visible-light conversion efficiency of 38.7 % is much higher than that of 3D bulk SnS_2. Wei *et al.*[23] also prepared the ultrathin SnS_2 nanosheets, in which the photocatalytic activity is significantly enhanced due to the 2D sheet-like nanostructure. Although the photocatalytic activity of single-layer SnS_2 is improved with respect to its bulk phase, there exists the restriction for the visible optical absorption and hydrogen production from solar water splitting.[24] More recently, in addition to explore the electronic and optical properties of SnS_2, doping of foreign species in pristine single-layer SnS_2 has been carried out to solve the above mentioned problems. An *et al.*[25] prepared transition metal Cu-doped SnS_2 nanosheet, in which the visible-light-driven activity is 7 times higher than blank SnS_2 nanosheets. Besides that, the n- and p-type anion doping was also investigated to understand the conductivity mechanism of SnS_2 nanosheets based on first principle calculations.[26] However, to the best of our knowledge, there have been no systematical reports about the hole doping at cation sites in single-layer SnS_2 until now. And the cation doping is usually easier realized than that of anion doping in experiments. It is very imperative to explore the optical mechanism of low valence metal doping single-layer SnS_2. Besides, Peng *et al.*[27] pointed out that there was a correlation between defect-induced ferromagnetism and hole doping for semiconductors. That is to say, the influence of cation-site doping-induced hole on the magnetism of single-layer SnS_2 also should be considered. Therefore, in the present work, the metal element X (X=Li, Mg, and Al) was chosen as dopant in single-layer SnS_2. Based on the density functional theory (DFT), the effects of X doping with different hole density on the electronic structure and optical properties of single-layer SnS_2 were systematically investigated. And the magnetic and photochemical behaviors of X-doped SnS_2 monolayer were detailed analyzed.

2. Computational methods

All the calculations were performed on the basis of DFT method with the projector augmented wave (PAW) pseudopotentials as implemented in the Vienna *ab initio*

Department of Applied Physics, Institute of Advanced Materials Physics, Tianjin Key Laboratory of Low Dimensional Materials Physics and Preparing Technology, Faculty of Science, Tianjin University, Tianjin 300072, People's Republic of China.
E-mail address: weizhou@tju.edu.cn; Tel.: +86 02227406852.

Simulation Package (VASP) code.[28,29] The Perdew-Burke-Ernzerhof (PBE) parametrization of the generalized gradient approximation (GGA) was employed to model the exchange and correlation interactions.[30] The valence electron configurations considered in this work were Li ($1s^2 2s^1$), Mg ($3s^2$), Al ($3s^2 3p^1$), Sn ($4d^{10} 5s^2 5p^2$) and S ($3s^2 3p^4$), respectively. For the supercell model, a 4×4×1 (48 atoms) single layer of SnS_2 supercell was used, and a vacuum space of 14 Å was added to eliminate interaction between the layers. A kinetic energy cutoff of 450 eV was adopted in the plane-wave expansions, and the Monkhorst-Pack *k*-point grid was 3×3×1 for Brillouin Zone integrations. A larger 5×5×1 (75 atoms) supercell was used to test the effects of finite size on the characteristics of doped SnS_2 monolayer. The formation energy obtained from the larger supercell only differs in a fraction of meV from the calculation using the 4×4×1 (48 atoms) supercell and the magnetic moments are similar to the results using the 4×4×1 supercell, which indicates that the supercell size adopted in our work is reasonable. To precisely reproduce the experimental band gap of SnS_2, the on-site coulomb interaction of U=9 eV was applied only to Sn 3d orbitals, which has also been reported in other literatures.[26,31] During the geometrical optimization, all atomic positions and lattice constants were relaxed until the residual forces on atoms were less than 0.01 eV/Å, and the convergence criterion of total energy was set to be 10^{-5} eV/atom. In addition, for the bulk SnS_2, the van der Waals interaction was considered by using Grimme's DFT-D2 method[32] to better describe the non-bonding interaction between the layers of bulk SnS_2.

3. Results and discussion

3.1. Structural optimization and formation energies

The crystal structure of bulk SnS_2 is firstly optimized with the PBE and PBE+*U* methods to probe the accuracy and applicability of the calculated parameters adopted in this work. The calculated structural parameters, bond lengths and band gaps E_g are summarized in Table 1. Compared to the results obtained from PBE calculations, the optimized lattice constants and the band gap by the PBE+*U* method are in much better agreement with the experimental values.[33] Moreover, we also perform the structural optimization of the single-layer SnS_2 using the PBE+*U* approach. The obtained lattice parameter (a = 3.481 Å), the S-Sn bond length (d_{S-Sn}=2.437 Å) and the band gap (E_g=2.240 eV) are also close to the reference data.[22] Therefore, the above calculated results indicate that the PBE+*U* method and the parameters adopted are reliable and believable.

The low valence metal X doping in the single-layer SnS_2 is modeled by replacing the Sn site with one X atom (X=Li, Mg, and Al) (X_{Sn}) in the supercell. The top view and side view of the optimized SnS_2 monolayer are shown in Fig. 1. In order to explore the bonding nature in X-doped single-layer SnS_2, the difference charge density near the dopant X is simulated and plotted in Fig. 2. For pure single-layer SnS_2 (Fig. 2(d)), there is apparently existence of covalent

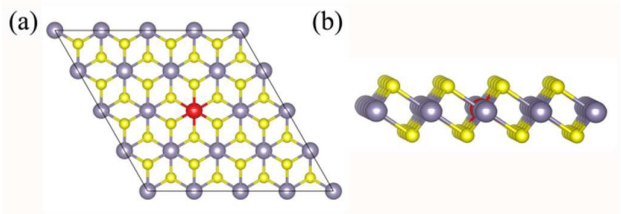

Fig. 1. The top view (a) and side view (b) of the optimized X-doped single-layer SnS_2. Yellow, dark and red spheres represent the S, Sn and X (X=Li, Mg, Al) atoms, respectively.

Table 1. Calculated structural parameters *a*, *c*, the bond lengths d_{Sn-S} and band gaps E_g for SnS_2 bulk and monolayer compared to those of experiments, respectively.

	Bulk (Monolayer)		
	PBE	PBE+*U*	Experiment
a (Å)	3.716 (3.645)	3.693 (3.481)	3.645 (3.700)
c (Å)	12.790 (—)	11.680 (—)	11.802 (—)
d_{Sn-S} (Å)	2.590 (2.579)	2.460 (2.437)	2.570 (2.600)
E_g (eV)	1.300 (1.574)	1.910 (2.240)	2.000 (2.230)

bonding between Sn and S atoms. For X-doped single-layer SnS_2, it is easy to find that the covalence character of X-S bond is gradually weakened while the ionic character is enhanced with the increase of hole density (from Fig. 2(c) to Fig. 2(a)). Furthermore, a significant ionic bonding behavior is observed between the Li and adjacent S atoms in Li-doped SnS_2. To further understand the chemical bond characteristic, the Bader charge[34] is calculated to analyze the charge transfer of every atom and the related X-S bond length is also presented, as summarized in Table 2. Positive and negative values indicate the loss and gain of charge, respectively. As can be seen, the valence electron on the Li atom is almost lost, which shows that obvious ionic bond character is easy to form in Li-doped SnS_2. Besides, the charge transfer rate presents a decreasing tendency with the decreasing hole density introduced by the doping, indicating that the electron transfer becomes increasingly unobvious and thereby resulting in the ionicity being weakened. This is in agreement with the above analysis of difference charge density. In addition, the results in Table 2 show that the bond length of the X-S (X=Li, Mg, and Al) is larger than that of Sn-S in the pristine single-layer SnS_2. It is well known that the strength of covalent bond is stronger than the ionic bond strength. Consequently, a possible reason for above conclusion is the existence of strong Sn-S covalent bond relative to Li (Mg)-S ionic bond and slightly weak Al-S covalent bond. In particular, combining the results of Table 2 and Fig. 2, it can be seen that the ionicity of the Li-S bond is much stronger than that of the Mg-S bond and thus leading to the shorter length for Li-S bond (2.540 Å) than the Mg-S bond length (2.567 Å).

In order to check the relative stability of the doped systems, the formation energy of X substitution with charged state q is calculated according to the following formula

$$E_{\mathrm{f}} = E(\mathrm{doped}) - E(\mathrm{pure}) + \sum n_{\mathrm{i}}\mu_{\mathrm{i}} + q(E_{\mathrm{F}} + \varepsilon_{\mathrm{VBM}} + \Delta v), \quad (1)$$

where E(doped) and E(pure) denote the total energies of the X-doped and pure single-layer SnS_2, respectively. The n_i (i=Sn, S and X)

Table 2. The Bader charge on the dopant X and its adjacent host atoms, as well as the X-S bond length $d_{X\text{-}S}$ (Å) are listed.

	Bader charge (e)					
Species	Sn	S	Li	Mg	Al	$d_{X\text{-}S}$ (Å)
Li:SnS_2	1.48	-0.67	0.84	—	—	2.540
Mg:SnS_2	1.48	-0.79	—	1.58	—	2.567
Al:SnS_2	1.48	-0.89	—	—	2.20	2.451
Pure	1.48	-0.74	—	—	—	2.437

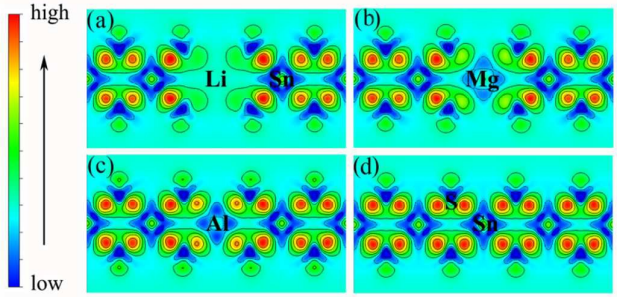

Fig. 2. Charge density difference near the dopant X and adjacent host atoms for (a) Li-, (b) Mg-, (c) Al-doped SnS_2, and (d) pure single-layer SnS_2, respectively.

is the number of atoms removed ($n_i > 0$) or added ($n_i < 0$) to the system, and μ_i is the chemical potential of the corresponding species. E_F is the Fermi energy level with respect to the energy position of the valence band maximum (ε_{VBM}) of the perfect single-layer SnS_2. Δv is the correction for the shift in average electron static potential of the 1s core level energy of a Sn atom (located far away from the defect site) between the neutral and charged states. As is well known, the formation energy depends on the growth conditions, which may be either Sn-rich or S-rich conditions. Conventionally, $\mu_i = \mu_i^{bulk} + \Delta\mu_i$, where μ_i^{bulk} is defined as the chemical potential of the elemental bulk solid, and $\Delta\mu_i$ denotes the chemical potential change of defects under different growth conditions. To avoid the precipition of SnS or Sn_2S_3 in SnS_2 phase, we set constraints on the chemical potentials of the type $m\Delta\mu_{Sn} + n\Delta\mu_S \leq \Delta H(Sn_mS_n)$,[35] in which $\Delta H(Sn_mS_n)$ is the formation enthalpy of the Sn_mS_n. And we obtain $-3.54\ \text{eV} \leq \Delta\mu_{Sn} \leq -0.06\ \text{eV}$ from the constraints. The value $\Delta\mu_{Sn} = -0.06\ \text{eV}$ corresponds to Sn-rich environment, whereas $\Delta\mu_{Sn} = -3.54\ \text{eV}$ characterizes the Sn-poor (S-rich) condition. Then μ_S is computed by the equilibrium condition in SnS_2: $\mu_{Sn} + 2\mu_S = \mu_{SnS_2}$. In addition, during the metal element X doping process, the restriction $m\Delta\mu_X + n\Delta\mu_S \leq \Delta H(X_mS_n)$ is further considered to prevent the formation of pahses Li_2S, MgS, and Al_2S_3 between the dopant and host atoms. According to Eq. (1), the neutral formation energies of X doping in single-layer SnS_2 are calculated under different conditions, as summarized in Table 3. The results show that the formation energies are lower under S-rich condition than that under Sn-rich condition for all doping cases, which implies that the doping is energetically favored under S-rich condition. In particular, there exists the lowest formation energy (E_f) when the Sn site is substituted by Al atom, which shows that the Al doping is easier to achieve compared with the Li and Mg doping. Besides, the E_f shows a decreasing trend with the decreasing hole density. The values of

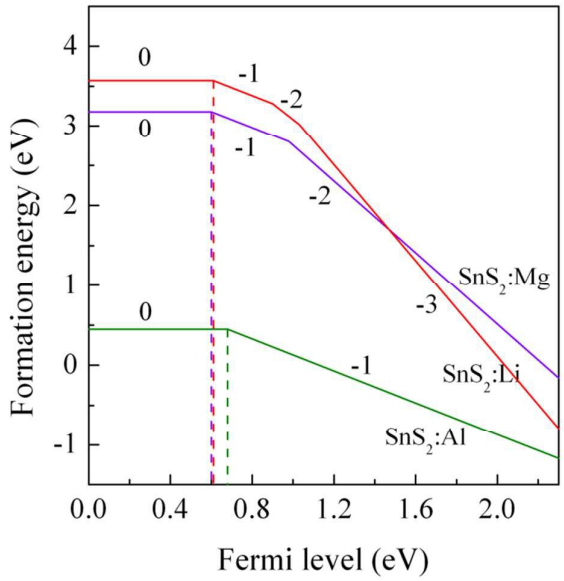

Fig. 3. The formation energies of X substitution (X_{Sn}) as a function of the Fermi level under the S-rich conditions.

E_f are in the order Li > Mg > Al, which is consistent with the order of ionic radius Li > Mg > Al but not in agreement with that of electronegativity Li (0.98) < Mg (1.31) < Al (1.61). This indicates that the influence of the ionic radius on the E_f exceeds the electronegativity so that the suitable ionic size plays a significant role on the feasibility of doping in single-layer SnS_2 in experiments. Meanwhile, to investigate the transition energy level between the neutral and charged defects, the formation energies of X-doped SnS_2 monolayer in different charged states under the S-rich growth conditions are calculated. Fig. 3 shows the formation energies as a function of the Fermi level E_F. It can be seen that the calculated (0/-1) transition energy levels are 0.61 eV, 0.60 eV and 0.68 eV above the VBM for Li, Mg and Al-doped single-layer SnS_2, respectively. These large values of transition energy level indicate that the X doping are deep acceptor impurities.

On the other hand, another issue that should pay attention is the formation of compensating defects, which can kill the holes carriers, for instance the formation of S vacancy (V_S). This hole killing mechanism has been already observed in the DFT+*U* studies of Cu-doped ZnS reported by Wang *et al.*.[36] Therefore, the complex defect of X_{Sn} + V_S is introduced to explore whether it is more favorable or challenging to form p-type characteristics in X-doped SnS_2 monolayer. Based on our calculations, the formation energies of the complex defect of X_{Sn} + V_S under S-rich conditions are 12.15 eV, 8.38 eV and 5.06 eV for Li, Mg and Al-doped SnS_2, respectively, which are much higher than that of separated neutral and charged X_{Sn} and V_S defects. It indicates that the V_S related defects are difficult to form in this situation. That is to say, this mechanism of hole compensation could be less pronounced in eliminating the holes carriers, thereby making the p-type doping for SnS_2 more favorable.

3.2. Electronic properties

To investigate effects of the doping on the characteristics of electronic structure of SnS_2, we present the total density of states (TDOS) and partial density of states (PDOS) of single-layer SnS_2 with X doping in Fig. 4. For comparison, the TDOS and PDOS of pure SnS_2

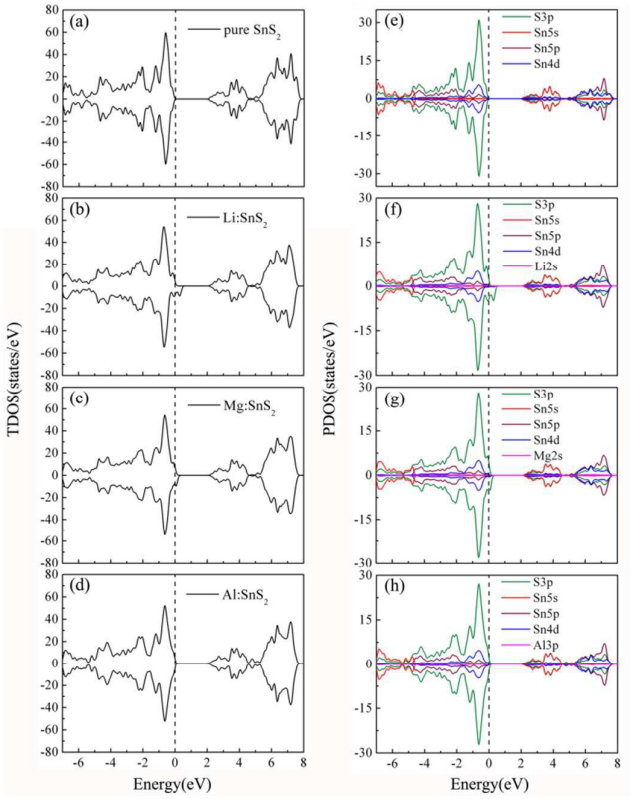

Fig. 4. Calculated TDOS (a)-(d) and PDOS (e)-(h) for pure and X-doped single-layer SnS_2. The vertical dash line indicates the E_F position.

monolayer are also calculated and displayed in Fig. 4(a) and 4(e). As can be seen, for the pristine single-layer SnS_2, the valence band (VB) mostly comprises the S 3p states, while the conduction band (CB) is mainly dominated by the hybridization of the S 3p and Sn 5s states. These results are in accordance with previous experimental and theoretical calculations,[22,26,33] which further indicates our calculated method is reasonable.

For metal elements Li and Mg doping in single-layer SnS_2, as shown in Fig. 4(b) and 4(c), the Fermi level (E_F) penetrates into the VB which indicates the p-type doping. The remarkable difference compared to the TDOS in Fig. 4(a) is that the incorporation of Li or Mg atom leads to the occurrence of defect states located above the valence band maximum (VBM). In addition, the PDOS of Fig. 4(f) and 4(g) show that the VB is still mainly dominated by the S 3p states and the CB is composed of the mixtures between S 3p and Sn 5s states. The Li or Mg dopant has almost little contribution to the constitution of the VB and CB, but it has a major influence on the adjacent atoms and changes their density of states distribution, thereby resulting in the hybridization between most S 3p orbital and a small part of Sn 4d orbital to form the defect states. These defect states are spin-polarized hole states, which makes the spin-up and spin-down TDOS asymmetric and causes the spin splitting. This implies that the single-layer SnS_2 doped with Li or Mg atom exhibits the magnetic ground states. Fig. 4(d) and 4(h) present the TDOS and PDOS of Al doping in the single-layer SnS_2. Similar to the Li and Mg doping cases, the components of VB and CB have no obvious changes, and the injection of Al atom also introduces

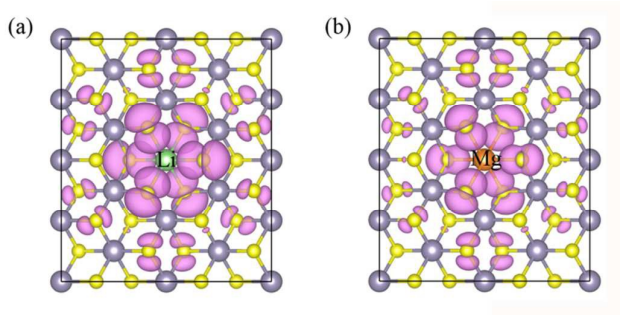

Fig. 5. Spin density distribution for Li-doped (a) and Mg-doped (b) single-layer SnS_2.

Table 3. The total magnetic moments M (μ_B), and formation energies E_f (eV) of X-doped single-layer SnS_2 under Sn-rich and S-rich conditions.

		E_f (eV)	
X-doped SnS_2	M (μ_B)	Sn-rich	S-rich
Li	3.00	5.18	3.57
Mg	1.75	4.92	3.18
Al	0	1.32	0.45

defect states of S 3p orbital character in the band gap. However, one can see that the spin-up and spin-down TDOS are symmetric, which suggests that the Al-doped single-layer SnS_2 exhibits non-magnetic ground states.

Table 3 lists the calculated total magnetic moments of doped systems. They are 3.00 μ_B, 1.75 μ_B, 0 μ_B for Li, Mg and Al doped SnS_2, respectively. We notice that the induced magnetic moments exhibit a monotonous decreasing trend, which may be ascribed to the decrease of hole density introduced by doping. In particular, although one hole is injected when the Al substitutes for Sn atom, the system is non-spin-polarized. The reason can be explained as follows. It is well known that the hole-doped system becomes spin polarized if it satisfies the Stoner criterion D (E_F)J > 1, where D (E_F) is the density of states at the Fermi level and J denotes the strength of the exchange interaction.[27] As can be seen from the TDOS, the values of D (E_F) are 8.94, 7.55 and 0.79 states/eV for Li, Mg, and Al doping, respectively. This value for Al doping is relatively small compared to that for Li and Mg doping. Consequently, the relative low D (E_F) will result in the Stoner criterion unlikely to be satisfied and thereby no magnetic moment in Al-doped single-layer SnS_2. In order to more intuitively observe the distribution of magnetic moments, the spin density distributions of Li and Mg doped systems are plotted in Fig. 5. Obviously, the spin density is mainly located on the nearest-neighbor and third-neighbor S atoms. The dopant Li or Mg has no spin polarization, which differs from the results of nonmetal doping in the SnS_2 monolayer[26] in which the induced spin polarizations are almost located on the defect site. The above results suggest that the dopant only plays a key role to provide S atom with holes and the spontaneous magnetization in the systems is induced by the hole of S 3p orbital character, which is consistent with the analysis of density of states.

3.3. Optical properties and photochemical energy conversion applications

As a promising material in the fields of photovoltaic devices and photocatalyst, it is indispensable to explore the effects of X doping on the optical properties of single-layer SnS_2. In our calculations, the optical absorption coefficient $\alpha(\omega)$ is obtained from the expression:

$$\alpha(\omega) = \sqrt{2}(\omega)\left[\sqrt{\varepsilon_1^2(\omega)+\varepsilon_2^2(\omega)}-\varepsilon_1(\omega)\right]^{1/2}, \quad (2)$$

where the imaginary part $\varepsilon_2(\omega)$ is directly associated with optical absorption and the real part $\varepsilon_1(\omega)$ is calculated from $\varepsilon_2(\omega)$ by the Kramer-Kronig transformation:[37]

$$\varepsilon_2(\omega) = \left(\frac{4\pi^2e^2}{m^2\omega^2}\right)\sum_{i,j}\int\langle i|MJ|\rangle^2 f_i(1-fj)\delta(E_f-E_i-\omega)d^3k. \quad (3)$$

In Fig. 6, we present the optical absorption spectra of X-doped single-layer SnS_2 as a function of photon energy. As a reference, the optical absorption coefficient of pure SnS_2 monolayer is also calculated and plotted in Fig. 6. Moreover, different optical incident light polarization directions, parallel (**E**$/\!/z$) and perpendicular (**E**$\perp z$) to the *z*-axis, are taken into account in this work for each doping case. As can be seen from Fig. 6, the characteristics of the optical absorption coefficients along **E**$/\!/z$ and **E**$\perp z$ directions are different, which indicates that the optical absorption presents anisotropic for doped systems. This is owing to the different dielectric response caused by the hexagonal structure of doped SnS_2. The optical anisotropy is also observed in $Sn_{1-x}Ti_xS_2$ ternary alloys.[31] Besides, for all doping cases, the absorption along **E**$\perp z$ direction is stronger than that along **E**$/\!/z$ direction. Thus, in order to enhance the efficiency of solar spectrum, the growth direction perpendicular to the *z*-axis should be chosen for the low valence metal X-doped single-layer SnS_2. In Fig. 6(a), we can see that the absorption edges of three doped systems exhibit obvious red-shift with respect to the pure SnS_2, which is associated with the decrease of band gap. It indicates that the low valence metal X doping is beneficial to improve the optical absorption in the visible light activity range. Furthermore, a broad absorbance peak from 0 to 2 eV occurs for each doping case, which is advantageous to improve the capacity of absorption in the low energy region. From the density of states analysis in Section 3.2, the appearance of the peak is directly related to the intraband transition caused by the unoccupied S 3p states located above the E_F. That is to say, the low valence metal X doping in single-layer SnS_2 can enhance the effective utilization of solar spectrum, especially in the near-infrared light.

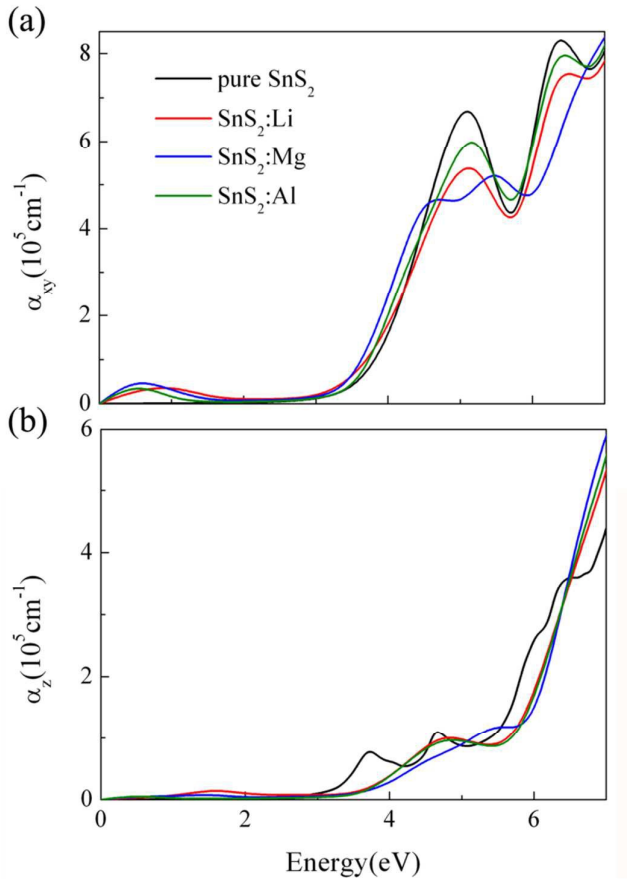

Fig. 6. The optical absorption coefficients as a function of photon energy along the directions of perpendicular (a) and parallel (b) to the *z* axis for X doping in single-layer SnS_2.

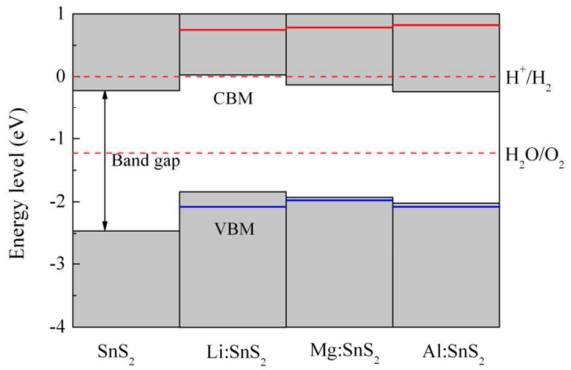

Fig. 7. Energy level diagram of pure and X-doped single-layer SnS_2 with respect to the standard reduction and oxidation potentials of water. The red and blue solid lines indicate the thermodynamic reduction and oxidation potentials, respectively.

In order to evaluate the effects of X-doped SnS_2 on the photocatalytic water splitting, the energy levels of doped systems are calculated and compared with the standard reduction and oxidation potentials of water. In our work, the energy zero is set to the reduction potential of H^+/H_2, and the valence and conduction band-edge positions are estimated from the calculated density of states. As a reference, the energy level diagram of pure single-layer SnS_2 is also given in Fig. 7. Apparently, the VBM of pristine SnS_2 monolayer is below the oxidation potential of H_2O/O_2 while the CBM does not lie across the reduction potential of H^+/H_2. This indicates that the pure single-layer SnS_2 is only favorable for oxygen evolution but not for hydrogen evolution, which agrees with the theoretical results of Ref. 24. For X- (Mg and Al) doped the single-layer SnS_2, the values of VBM lie more negative than the oxidation level of water and the CBM values still lie within the reduction level of water, which shows that they are active only for photo-oxidation of water. However, for Li doping in SnS_2, the VBM lie more negative than the oxidation potential of H_2O/O_2 and the CBM is about 0.03 eV higher than the reduction potential of H^+/H_2, which indicates that the doped system is beneficial for both the photo-reduction and photo-oxidation of water. Furthermore, the stability of semiconductors in the aqueous solution is also important for the

photocatalytic ability of materials, in addition to the band edge alignment. As reported by Wang *et al.*,[38] whether the semiconductor is resistant to the photocorrosion depends on the alignment of thermodynamic oxidation (φ^{ox}) and reduction potentials (φ^{re}) relative to the water redox potentials. The φ^{ox} and φ^{re} should be taken into account for the choice of candidate photocatalytic materials. Therefore, in order to investigate the stability of doped systems in aqueous solution, the thermodynamic potentials were estimated with the model proposed by Wang *et al*., as shown in Fig.7. As can be seen, the φ^{ox} is lower than the oxidation potential of H_2O/O_2 for Mg (or Al)-doped single-layer SnS_2, which shows that this material is stable with respect to the hole oxidation. For Li-doped SnS_2, the φ^{ox} is lower than the oxidation potential of H_2O/O_2 and the φ^{re} is higher than the reduction potential of H^+/H_2, indicating this doped system is stable with respect to both the hole oxidation and electron reduction. Thus, the Li doping in single-layer SnS_2 is expected to be a potential candidate for overall water splitting under visible light radiation.

4. Conclusions

The first-principles calculations were performed to investigate the electronic and optical properties of low valence metal X (X=Li, Mg and Al) doping in single-layer SnS_2. The results show that the doping is energetically favored under S-rich condition with respect to Sn-rich condition, and the Al doping is easier to realize than Li and Mg doping. There is an ionic bonding character for Li-S and Mg-S bonds while covalent bonding behavior for Al-S bond. The defect states of S 3p character are introduced in the band gap, leading to a total magnetic moment of 3.00 μ_B and 1.75 μ_B for Li and Mg-doped SnS_2, respectively. However, the system with Al doping exhibits the non-magnetic ground states, which is due to the low hole density around the Fermi level. The calculations of optical properties show that the optical absorption along the *xy* plane is stronger than that along *z* direction, and the red shift of absorption edges are observed for all doping cases, which accordingly improves the photocatalytic ability in visible light range. Also, the effective utilization in the near-infrared light is enhanced because of the defect states. In addition, the Li doping in single-layer SnS_2 is expected to be a potential candidate for overall water splitting whereas the Mg and Al doping is suitable only for oxygen evolution.

Acknowledgements

This work was supported by the National Natural Science Foundation of China (51074112) and (11247224), and the supercomputing resources were supported by High Performance Computing Center of Tianjin University, China.

References

1 K. S. Novoselov, A. K. Geim, S. V. Morozov, D. Jiang, Y. Zhang, S. V. Dubonos, I. V. Grigorieva and A. A. Firsov, *Science*, 2004, **306**, 666–669.
2 P. Avouris, Z. Chen and V. Perebeinos, *Nat. Nanotechnol.*, 2007, **2**, 605.
3 A. K. Geim and K. S. Novoselov, *Nat. Mater.*, 2007, **6**, 183.
4 C. N. R. Rao, K. Biswas, K. S. Subrahmanyam and A. Govindaraj, *J. Mater. Chem.*, 2009, **19**, 2457.
5 C. N. R. Rao, A. K. Sood, K. S. Subrahmanyam and A. Govindaraj, *Angew. Chem. Int. Ed.*, 2009, **48**, 7752.
6 D. Golberg, Y. Bando, Y. Huang, T. Terao, M. Mitome, C. C. Tang and C. Y. Zhi, *ACS Nano*, 2010, **4**, 2979-2993.
7 A. Pakdel, X. B. Wang, C. Y. Zhi, Y. Bando, K. Watanabe, T. Sekiguchi, T. Nakayama and D. Golberg, *J. Mater. Chem.*, 2012, **22**, 4818-4824.
8 C. Xia, Y. Peng, S. Wei and Y. Jia, *Acta Mater.*, 2013, **61**, 7720-7725.
9 C. H. Ho, M. H. Hsieh and C. C. Wu, *Rev. Sci. Instrum.*, 2006, **77**, 113102.
10 Y. C. Huang, C. Y. Ling, H. Liu, S. Y. Wang and B. Y. Geng, *J. Phys. Chem. C*, 2014, **118**, 9251-9260.
11 R. Wei, J. Hu, T. Zhou, X. Zhou, J. Liu and J. Li, *Acta Mater.*, 2014, **66**, 163-171.
12 D. M. Guzman and A. Strachan, *J. Appl. Phys.*, 2014, **115**, 243701.
13 W. Z. Bao, X. H. Cai, D. Kim, K. Sridhara and M. S. Fuhrer, *Appl. Phys. Lett.*, 2013, **102**, 042104.
14 Y. Ge, W. Wan, W. Feng, D. Xiao and Y. Yao, *Phys. Rev. B*, 2014, **90**, 035414.
15 S. Das , H. Y. Chen , A. V. Penumatcha and J. Appenzeller , *Nano Lett.*, 2013, **13**, 100.
16 P. Chen, Y. Su, H. Liu and Y. Wang, *ACS Appl. Mater. Interfaces*, 2013, **5**, 12073-12082.
17 D. Ma, H. Zhou, J. Zhang and Y. Qian, *Mater. Chem. Phys.*, 2008, **111**, 391-395.
18 Y. C. Zhang, Z. N. Du, S. Y. Li and M. Zhang, *Appl. Catal. B.*, 2010, **95**, 153-159.
19 J. Yu, C. Y. Xu, F. X. Ma, S. P. Hu, Y. W. Zhang and L. Zhen, *Appl. Mater. Interfaces*, 2014, **6**, 22370-22377.
20 S. H. Chaki, M. P. Deshpande, D. P. Trivedi, J. P. Tailor, M. D. Chaudhary and K. Mahato, *Appl. Nanosci.*, 2013, **3**, 189.
21 J. Seo, J. Jang, S. Park, C. Kim, B. Park and J. Cheon, *Adv. Mater.*, 2008, **20**, 4269.
22 Y. Sun, H. Cheng, S. Gao, Z. Sun, Q. Liu, Q. Liu, F. Lei, T. Yao, J. He, S. Wei and Y. Xie, *Angew. Chem. Int. Ed.*, 2012, **51**, 8727.
23 R. Wei, J. Hu, T. Zhou, X. Zhou, J. Liu and J. Li, *Acta Mater.*, 2014, **66**, 163-171.
24 H. L. Zhuang and R. G. Hennig, *Phys. Rev. B*, 2013, **88**, 115314.
25 X. An, C. Y. Jimmy and J. Tang, *J. Mater. Chem. A*, 2014, **2**, 1000.
26 C. X. Xia, Y. T. Peng, H. Zhang, T. X. Wang, S. Y. Wei and Y. Jia, *Phys. Chem. Chem. Phys.*, 2014, **16**, 19674.
27 H. W. Peng, H. J. Xiang, S. H. Wei, S. S. Li, J. B. Xia and J. B. Li, *Phys. Rev. Lett.,* 2009, **102**, 017201.
28 G. Kresse and J. Hafner, *Phys. Rev. B*, 1993, **47**, 558.
29 G. Kresse and J. Furthmuller, *Phys. Rev. B*, 1996, **54**, 11169.
30 J. P. Perdew, K. Burke and M. Ernzerhof, *Phys. Rev. Lett.*, 1996, **77**, 3865-3868.
31 C. Xia, J. An, T. Wang, S. Wei and Y. Jia, *Acta Mater.*, 2014, **72**, 223-228.
32 S. Grimme, *J. Comput. Chem.*, 2006, **85**, 1787-1799.
33 S. K. Arora, D. H. Patel and M. K. Agarwal, *Cryst. Res. Technol.*, 1993, **28**, 623-627.
34 R. F. W. Bader, *Atoms in Molecules: a Quantum Theory*, Oxford University Press, New York, 1990.
35 B. D. Malone, A. Gali and E. Kaxiras, *Phys. Chem. Chem. Phys.*, 2014, **16**, 26176-26183.
36 H. H. Pham, G. T. Barkema and L.-W. Wang, Phys. Chem. Chem. Phys., 2015, **17**, 26270-26276.
37 C. M. I. Okoye, *J. Phys.: Condens. Matter*, 2003, **15**, 5945.
38 S. Chen and L.-W. Wang, Chem. Mater., 2012, **24**, 3659-3666.